Functionalized Au_{22} Clusters: Synthesis, Characterization, and Patterning

E. S. Shibu,[†] B. Radha,[§] P. K. Verma,[||] P. Bhyrappa,*[,‡] G. U. Kulkarni,[§] S. K. Pal,[||] and T. Pradeep*[,†]

DST Unit on Nanoscience (DST UNS), Department of Chemistry and Sophisticated Analytical Instrument Facility and Department of Chemistry, Indian Institute of Technology, Madras, Chennai 600 036, India, Chemistry and Physics of Materials Unit and DST UNS, Jawaharlal Nehru Centre for Advanced Scientific Research, Jakkur P.O., Bangalore 560 064, India, and Unit for Nanoscience and Technology, Department of Chemical, Biological and Macromolecular Sciences, Satyendra Nath Bose National Centre for Basic Sciences, Kolkata, India

ABSTRACT We synthesized fluorescent, porphyrin-anchored, Au_{22} clusters in a single step, starting from well-characterized Au_{25} clusters protected with glutathione (−SG) by a combined core reduction/ligand exchange protocol, at a liquid−liquid interface. The prepared cluster was characterized by UV/vis, photoluminescence, X-ray photoelectron spectroscopy (XPS), scanning electron microscopy, elemental analysis, and matrix-assisted laser desorption ionization mass spectrometry. The absence of a 672 nm intraband transition of Au_{25} and the simultaneous emergence of new characteristic peaks at 520 and 635 nm indicate the formation of the Au_{22} core. An increase in the binding energy of 0.4 eV in Au 4f core-level peaks confirmed the presence of a reduced core size. Quantitative XPS confirmed the Au/S ratio. The presence of a free base, tetraphenylporphyrin (H_2TPPOAS−), on the Au_{22} core was confirmed by fluorimetric titrations with Cu^{2+} and Zn^{2+} ions. From all of these, the composition of the cluster was determined to be $Au_{22}[(-SG)_{15}(-SAOPPTH_2)_2]$, which was supported by mass spectrometry and elemental analysis. We utilized the fluorescence nature of these water-soluble clusters for the fabrication of fluorescent patterns by soft lithography. The patterns were studied using tapping-mode atomic force microscopy and confocal fluorescence imaging.

KEYWORDS: Au_{22} • core reduction/ligand-exchange reaction • tetraphenylporphyrin • fluorescent patterns • soft lithography

INTRODUCTION

Noble metal nanoclusters of gold and silver of less than 2 nm cores are important in various fields of science and technology. The interest is mainly due to their unique properties such as photoluminescence (PL) (1−3), ferromagnetism (4), optical chirality (5), etc. They are also good candidates for applications such as catalysis (6, 7), nanoelectronics (8), sensing (9−11), bioanalysis (12), etc. Semiconductor nanocrystals or quantum dots have unique optical properties that make them potential candidates as luminescent probes for biological applications ranging from immunoassays to live cell imaging (13−17). However, high toxicity associated with some quantum dots such as CdSe limits their applications in biology (18) particularly in live cell imaging, in vivo diagnosis, etc., although approaches to reduce the toxicity have been suggested (18, 19).

Fluorescent clusters of gold and silver are less toxic compared to semiconductor quantum dots. This makes them potential labels for biologically motivated experiments (20−22). These clusters, also called quantum clusters, are a new class of materials with a definite number of atoms in their core. On the basis of the number of gold atoms present in their core, several clusters such as Au_8 (23−26), A_{11} (27), Au_{13} (28), Au_{55} (29), etc., have been synthesized. Dickson and co-workers reported strongly photoluminescent silver clusters generated by the irradiation of UV light on oxidized thin films of silver (30). The first attempt to make highly fluorescent gold clusters inside the poly(amidoamine) (PAMAM) dendrimer cavity was by the same group in 2003 (24). They have synthesized a series of gold clusters inside the PAMAM cavity with high quantum yields (23−25). Among these gold clusters, Au_8 is highly luminescent and blue-emitting (24). However, these clusters are not free because they are made inside the cavity. Several photochemical and chemically reduced water-soluble fluorescent silver clusters have been reported in recent years that are encapsulated in DNA and protein templates (31), in PAMAM cavities (32), in polymer microgels (33), and in microemulsions (34). All of these clusters synthesized inside the cavity/templates show high quantum yields, which make them good candidates for biological applications.

The first attempt to prepare stable and size-separated gold nanoclusters protected with glutathione (GSH) was by Whetten and co-workers (35). Mass spectrometry confirmed that $Au_{28}(SG)_{16}$ was the most abundant species in the synthesis (5). In the recent past, a series of −SG-protected gold clusters with well-defined compositions have been synthesized (36). The different fractions were separated utilizing poly(acrylamide) gel electrophoresis (PAGE). The

* Corresponding author. Fax: + 91-44 2257-0545. E-mail: pradeep@iitm.ac.in (T.P.), bhyrappa@iitm.ac.in (P.B.).
Received for review May 23, 2009 and accepted August 27, 2009
[†] DST UNS, Department of Chemistry and Sophisticated Analytical Instrument Facility, Indian Institute of Technology.
[‡] Department of Chemistry, Indian Institute of Technology.
[§] Jawaharlal Nehru Centre for Advanced Scientific Research.
[||] Satyendra Nath Bose National Centre for Basic Sciences.
DOI: 10.1021/am900350r

Scheme 1. Schematic Representation of the Synthesis of H_2TPPOASH

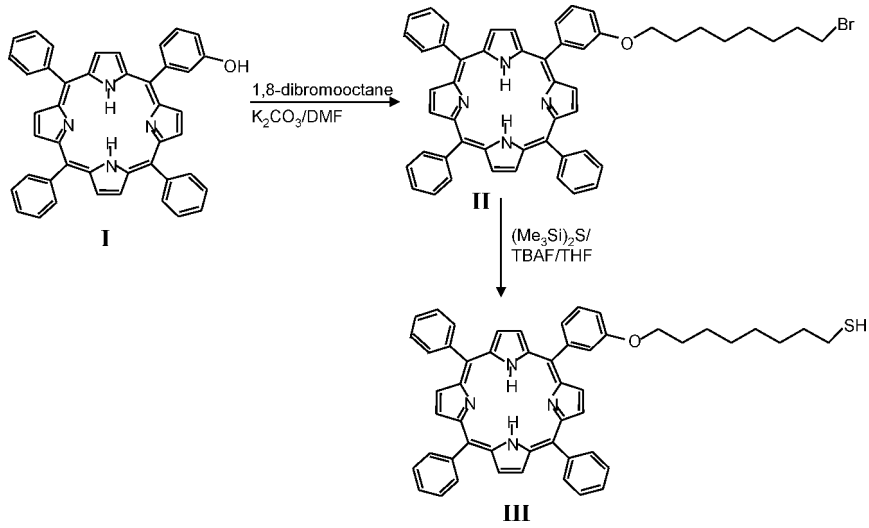

molecular compositions of these clusters were characterized by electrospray ionization mass spectrometry (ESI-MS). Tsukuda et al. (36) characterized the elemental composition of all of the separated entities by ESI-MS and confirmed that the most abundant species is $Au_{25}(SG)_{18}$ and not $Au_{28}(SG)_{16}$, as suggested originally (5). The ligand-exchange reaction of phosphine-stabilized gold clusters (Au_{11}) with GSH gave only $Au_{25}SG_{18}$ in large yield, suggesting that it is the most stable one among the thiolated clusters from this class (37). Chemical-etching reaction with excess GSH was used to synthesize $Au_{25}SG_{18}$ in gram scale (38). The stability of such clusters has been studied in detail (39). The crystal structure of the Au_{25} core with a $-SC_2H_4Ph$ ligand was solved recently (40). Incorporation of the desired molecules on the Au_{25} core brings about some selected functionality. With this interest, we functionalized Au_{25} with a variety of molecules (41, 42). The ligand-exchange reaction of mercaptobutanol with GSH was studied by ^{1}H NMR, and exchange kinetics was found to be first-order (41). Dansylglutathione-functionalized Au_{25} showed excellent energy transfer from dansyl to the metal core (43). The main drawback of Au_{25} and its variously functionalized clusters is their low quantum yield (1.9×10^{-3}). Recently, blue-emitting GSH-capped Au_8 with high quantum yield was synthesized in gram scale (44). Tholate-protected Au_{20} clusters were reported recently by Jin and coworkers (45). Luminescent silver clusters were synthesized by interfacial etching (46). Highly fluorescent gold clusters were synthesized inside bovine serum albumin (47).

In this article, we are presenting a new synthetic route for near-infrared (NIR)-emitting clusters with high quantum yield, starting from a stable, well-characterized subnanocluster, $Au_{25}SG_{18}$. The synthetic protocol includes an in situ core reduction combined with ligand-exchange reaction. The new cluster was characterized by UV/vis, steady-state fluorescence, matrix-assisted laser desorption ionization time-of-flight mass spectrometry (MALDI-TOF MS), scanning electron microscopy (SEM), X-ray photoelectron spectroscopy (XPS), elemental analysis, and lifetime measurements. Further, we have created micropatterns of these clusters. Micropatterning fluorescent molecules or cluster species is of great significance in the development of high-density optical memories and photonic switches (48, 49), miniaturized biosensors (50), and markers for biological microarray production (51) as well as for studying the nature of intercellular communication in patterned cells (52, 53).

One of the simple and robust methods for micropatterning various materials is micromolding in capillaries (54). This method can be extended to produce high-resolution nanoscale patterns (55). Besides being simple, it offers the advantage of a large area patterning ability in less time, which is economical as well (56). The patterns thus fabricated have been characterized by atomic force microscopy (AFM) and confocal fluorescence mapping. The patterns are highly fluorescing and exhibit extreme conformity with the stamp geometry. This will help to utilize these clusters as fluorescent markers in soft lithography and associated applications.

EXPERIMENTAL SECTION

Materials. All of the chemicals were commercially available and used without further purification. $HAuCl_4 \cdot 3H_2O$, methanol (GR grade), ethanol (GR grade), and GSH (γ-Glu-Cys-Gly, MW = 307) were purchased from SRL Chemical Co. Ltd., India. $NaBH_4$ (>90%) and MB (MW = 106) were purchased from Sigma Aldrich. Deionized (DI) water with resistivity >18 MΩ/cm was used for all of the experiments. Tetraphenylporphyrinthiol (H_2TPPOASH, **III**) was synthesized using a reported procedure (57−59). The precursor porphyrin, 5-(3-hydroxyphenyl)-10,15,20-triphenylporphyrin, H_2TPP (m-OH, **I**), was prepared using a reported method (57). 1,8-Dibromooctane, tetrabutylammonium fluoride, and hexamethyldisilathiane were purchased from Sigma-Aldrich (India). Dimethylformamide (DMF), K_2CO_3, and $CHCl_3$ were of analytical grade.

Synthesis of Compound III. The schematic of the compound **III** synthesis is given in Scheme 1. H_2TPPOABr (**II**) was synthesized by the reaction of compound **I** with 1,8-dibromooctane in DMF in the presence of K_2CO_3 using a modified literature procedure (58). A mixture of compound **I** (0.125 g, 0.19 mmol), 1,8-dibromooctane (0.30 mL, 0.9 mmol), and anhydrous K_2CO_3 (0.25 g) in DMF (30 mL) was stirred at 60 °C under an inert atmosphere for 4 h. Then, the reaction mixture was poured into 100 mL of distilled water and filtered through a sintered-glass

(G4) crucible. The residue was washed with distilled water followed by CH_3OH (2 × 10 mL). The product mixture was chromatographed on a silica gel column using $CHCl_3$ as the eluent. The fast-moving fraction was collected and evaporated to dryness to yield the desired product (0.10 g, 85%). The product was characterized by ^1H NMR, electronic absorption, and MS methods. Electronic absorption in CH_2Cl_2 [λ_{max}, nm (log ϵ)]: 422 (5.30), 516 (4.23), 554 (4.16), 591 (3.82), 646 (3.76). ^1H NMR in $CDCl_3$: 8.87 ppm (m, 8H, β-pyrrole H), 8.24 (m, 8H, *o*-phenyl H), 7.79 (m, 11H, *m*- and *p*-phenyl H), 4.14 (t, 2H, $O-CH_2$), 3.41 (t, 2H, (CH_2-Br)), 1.84 (m, 4H, $(CH_2)_2$), 1.35−1.46 (m, 8H, $(CH_2)_4$), 1.45 (m, 2H, CH_2). ESI-MS in a methanol/tetrahydrofuran (THF) mixture (*m*/*z*): 823.0 (calcd, 821.86).

The synthesis of compound **III** was carried out using a variant of the reported method (59). To a stirred solution of compound **II** (0.065 g, 0.073 mmol), in freshly distilled THF (40 mL), was added hexamethyldisilathiane (0.04 mL, 0.2 mmol) under an inert atmosphere; tetrabutylammonium fluoride (0.05 g) was added subsequently, and the solution was stirred for a period of 3 h. To the reaction mixture was added distilled water (50 mL), and the resulting solution was stirred for a further period of 30 min. Then the organic layer was separated and rotary-evaporated to dryness. The purple residue was redissolved in a minimum amount of $CHCl_3$ and chromatographed on a silica gel column using a $CHCl_3$/hexane (4:1, v/v) mixture. The first fraction was collected and rotary-evaporated to dryness. The sample was dried under a vacuum at 80 °C for 6. The yield of the product was found to be 0.040 g (55%). Electronic absorption spectrum in CH_2Cl_2 [λ_{max}, nm (log ϵ)]: 421 (5.21), 517 (4.16), 556 (4.20), 590 (3.84), 645 (3.78). ^1H NMR in $CDCl_3$: 8.88 ppm (m, 8H, β-pyrrole H), 8.21 (m, 8H, *o*-phenyl H), 7.75 (m, 11H, *m*- and *p*-phenyl H), 4.08 (t, 2H, $O-CH_2$), 2.95 (m, 2H, (CH_2-S)), 1.81 (m, 2H, CH_2), 1.70 (m, 2H, (CH_2)), 1.25−1.32 (m, 8H, $(CH_2)_4$). ESI-MS in a methanol/THF mixture (*m*/*z*): 776.0 (calcd, 775.02).

Synthesis of Au@SG. To a 50 mL methanolic solution (0.25 mM) of $HAuCl_4 \cdot 3H_2O$ was added 1.0 mM GSH (1:4 ratio; the total volume of methanol was 50 mL). The mixture was cooled to 0 °C in an ice bath for 30 min. An aqueous solution of $NaBH_4$ (0.2 M, 12.5 mL), cooled to 0 °C, was injected rapidly into the above mixture under vigorous stirring. The mixture was allowed to react for another 1 h. The resulting precipitate was collected and washed repeatedly with methanol through centrifugal precipitation. Finally, the Au@SG precipitate was dried and collected as a dark-brown powder (36, 38).

Synthesis of $Au_{25}SG_{18}$ from Crude Au@SG. The above powder was dissolved in 50 mL of 1.0 mM SG (in water) and heated at 55 °C in a test tube for about 12 h using an EYELA process station. The solid material formed was centrifuged out, and $Au_{25}SG_{18}$ was precipitated from the solution by the addition of methanol. The precipitate was repeatedly washed with methanol and finally with ethanol. The precipitate was dried in a vacuum and obtained as a brown powder (38, 39, 41, 43).

Synthesis of Porphyrin-Anchored Au_{22} from Au_{25} (Core Reduction/Ligand-Exchange Reaction). About 20 mg of Au_{25} was dissolved in 5 mL of DI water and stirred for a few minutes. To this suspension was added the compound **III** solution (2 mg in 5 mL of toluene), and the resulting solution was stirred for 48 h. After completion of the reaction (by checking the fluorescence of the solution under a UV lamp), toluene was evaporated using a rotary pump. The aqueous solution was centrifuged at 20 000 rpm for 10 min at 15 °C. The supernatant solution was carefully decanted and dried using a EYELA freeze dryer. The solid product was purified using PAGE. PAGE was done using a gel electrophoresis unit with a 1 mm thick spacer (Biorad, Miniprotein Tetra cell). The total contents of the acrylamide monomers were 30% [bis(acrylamide):bis(acrylamide) = 7:93] and 3% [bis(acrylamide):bis(acrylamide) = 6:94] for the separating and stacking gels, respectively. The eluting buffer consisted of 192 mM glycine and 25 mM tris(hydroxymethylamine). The crude Au_{22} was dissolved in a 5% (v/v) glycerol/water solution (1.0 mL) at a concentration of 15 mg/mL. The sample solution (1.0 mL) was loaded onto a 1 mm gel and eluted for 6 h at a constant voltage of 120 V. The gel containing the cluster sample was cut out, ground, and dipped in ice-cold distilled water (2 mL) overnight. Subsequently, the mixture was centrifuged at 20 000 rpm for 30 min at −10 °C to remove the gel lumps suspended in the solution. The sample was freeze-dried, and the pure Au_{22} powder was collected. The cluster was characterized by UV/vis, fluorescence, XPS, SEM, elemental analysis, and lifetime measurements. Because transmission electron microscopy does not give detailed information on subnanoclusters and in view of the beam-induced coalescence of clusters leading to nanoparticles (41), this study was not attempted. A schematic of the cluster synthesis is given in Scheme 2. The photograph shows the intense red emission from the aqueous solution of the new cluster under a UV lamp. Au_{25} does not appear fluorescent to the naked eye at this concentration and in water at room temperature because its quantum yield is 1.9×10^{-3}. The molecular structure of GSH is also given in the scheme.

Preparation of the PDMS Stamp and Fluorescent Patterns. The basic principle of the micropatterning technique is to create a stamp having the desired patterns. The structure from which the stamp is derived is known as the "master". It can be fabricated by any technique that is capable of producing well-defined structures of relief on a surface. In our studies, we used poly(dimethylsiloxane) (PDMS) as a stamp and a compact disk (CD) as the "master". Once the PDMS stamp is formed, it is placed on a substrate, which thus forms a network of straight and continuous channels. Details of the PDMS stamp preparation are given in the Supporting Information.

The patterning of fluorescent Au_{22} consisted of three steps (see Scheme 3). The PDMS stamp was kept on the substrate so that the relief features on the surface of the stamp formed a network of straight and continuous channels (~950 nm wide). Approximately, 100 μL of a Au_{22} solution in ethanol (10^{-4} M) was dropped at one edge of the stamp to fill the channels spontaneously by capillary action. The whole setup was left undisturbed for solvent evaporation for 60 min on the surface of a heating plate at 50 °C. Afterward, the stamp was removed, leaving behind the fluorescent patterns on the substrate. This pattern was used for all of the measurements.

Methods. UV/vis spectra were recorded using a Perkin-Elmer Lambda 25 spectrophotometer. The photoexcitation and fluorescence studies were done using a NanoLog Horiba Jobin-Yvon spectrofluorimeter with a 100 W xenon lamp as the excitation source, at a scan speed of 240 nm/s. The band pass for both excitation and emission monochromators was kept at 5 nm. Solid-state emission and inherent fluorescence images were performed on a Witec GmbH confocal Raman spectrometer equipped with 532 nm excitation. The excitation laser was focused using a 100× objective, and the signal was collected in a backscattering geometry and guided to a Peltier-cooled charge-coupled-device (CCD) detector. The sample was mounted on a piezo-equipped scan stage to enable spectral imaging. Single-spot spectra were also acquired using the same grating but with larger integration times. For improved resolution and to ascertain the peak positions, a grating with 1800 grooves/mm was also used while acquiring single-spot spectra. The effective scan range of the spectrometer was 0−9000 cm^{-1} (which amounts to a wavelength maximum of 1020.70 nm for 532 nm excitation), with the detection efficiency falling above 750 nm. For spectral imaging, the desired area was partitioned into 10 000 squares (an imaginary 100 × 100 matrix drawn over it), with each square representing a sampling point and, consequently, a pixel for the image. The typical signal acquisition time at each pixel of the image was 0.1 s. The intensities of the desired portion of the spectra, collected over all of the pixels, were

Scheme 2. Schematic Representation of the Formation of NIR-Emitting Au_{22} Clusters from Parent Au_{25} by Simultaneous Core Reduction and Ligand Exchange[a]

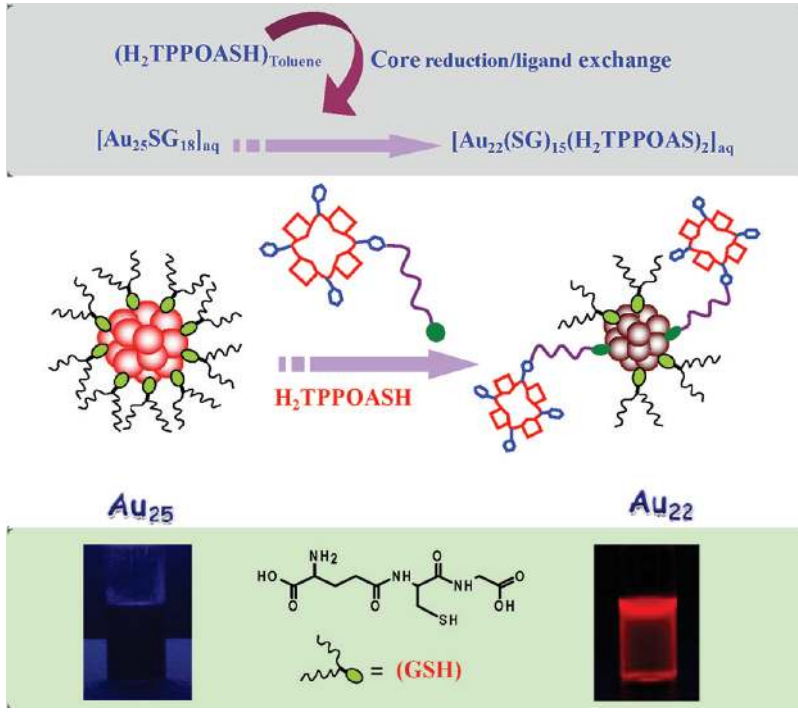

[a] Photographs show the emission of Au_{25} and the new cluster in an aqueous medium under a UV lamp at room temperature. The molecular structure of GSH is also given.

Scheme 3. Schematic Showing the Preparation of the PDMS Stamp from a CD and an AFM Image of the Stamp[a]

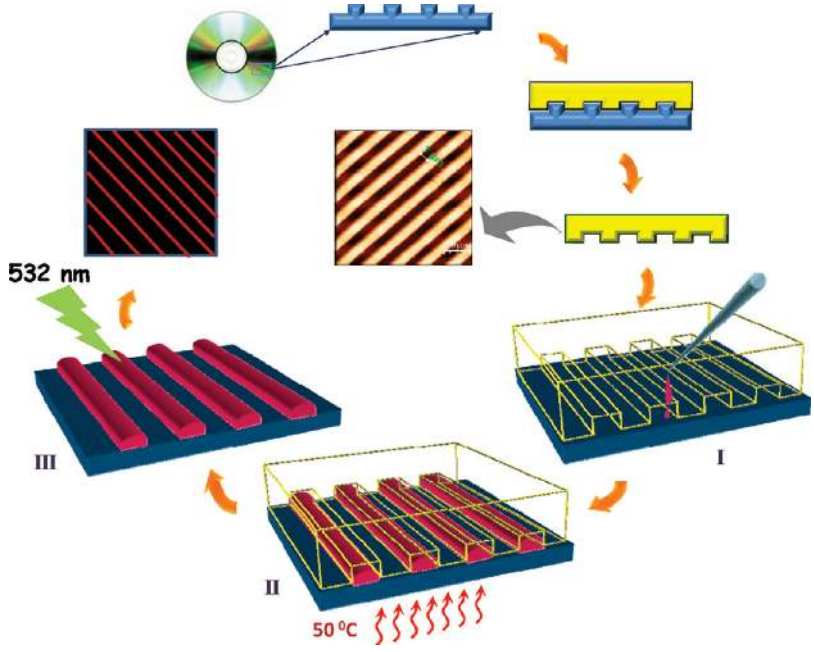

[a] Step I shows the expanded view a PDMS stamp. Incubation of Au_{22} in the microchannels of the PDMS stamp and the subsequent processes are given in steps I and II. Step III shows the patterns of Au_{22}.

compared by Scan CTRL Spectroscopy Plus Version 1.32 software, to construct color-coded images. Spectral intensities acquired over a predefined area were automatically compared to generate color-coded images. In the images, the red-coded regions are regions with maximum fluorescence intensities and the regions shown in black are those with minimum signal intensities. XPS measurements were done using an Omicrometer Nanotechnology spectrometer with polychromatic Al Kα X-rays ($h\nu$ = 1486.6 eV). At least 10 spectra in the desired binding energy (BE) range were collected, and an average was taken. The samples were spotted as drop-cast films on the sample stub and dried under a vacuum. The X-ray flux was adjusted to reduce the beam-induced damage of the sample. The energy resolution of the spectrometer was set at 1.1 eV at

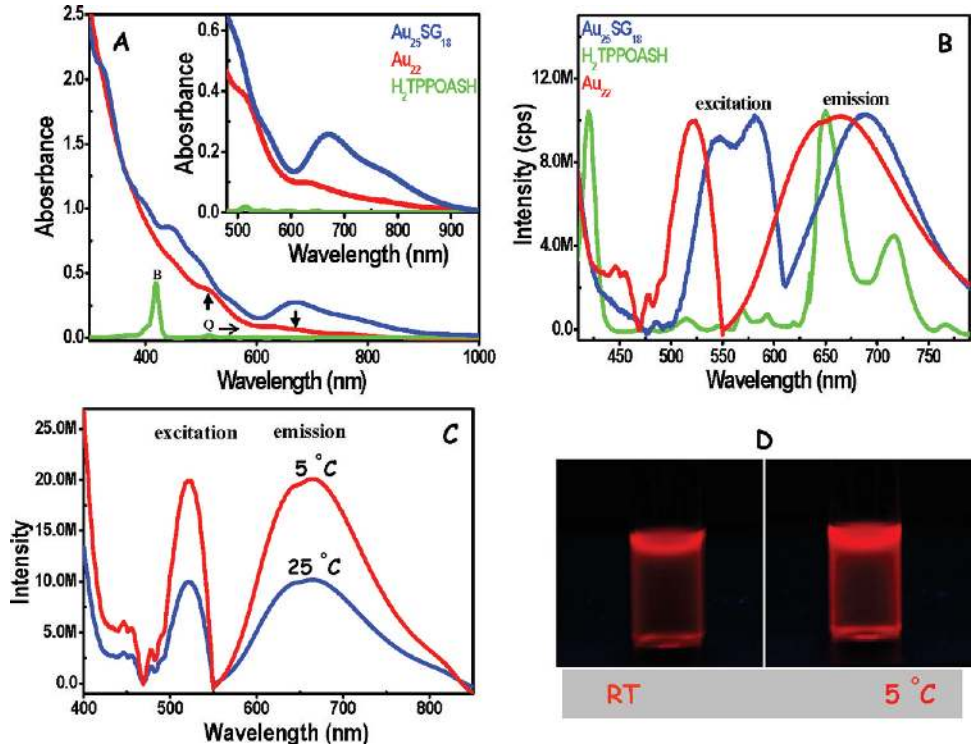

FIGURE 1. (A and B) UV/vis and PL spectra of Au_{25}, Au_{22}, and H_2TPPOASH (the B and Q bands of H_2TPPOASH are labeled). The inset in part A shows the expanded view of the HOMO−LUMO transitions of these clusters along with the Q bands of porphyrin. The emission of Au_{22} merged with the H_2TPPOASH emission. The peak at 468 nm in the excitation spectrum of the cluster confirms the presence of H_2TPPOASH. (C) Temperature-dependent PL spectra of Au_{22} at room temperature and 5 °C. The corresponding photographs of the solutions under a UV lamp are given in part D.

a pass energy of 50 eV. The BE was calibrated with respect to C 1s (285.0 eV). Fluorescence transients were measured and fitted by using a commercially available spectrometer (Lifespec-ps) from Edinburgh Instruments, Livingston, U.K. [80 ps instrument response function (IRF)]. AFM measurements were done using Dimension 3100 SPM with a NS IV controller (Veeco Instruments Inc., Plainview, NY), in the tapping mode. Standard Si_3N_4 cantilevers were used for normal topography imaging. SEM and energy-dispersive analysis of X-rays (EDAX) were carried out with a FEI QUANTA 200. The ^{1}H NMR spectrum of H_2TPPOASH was measured with a Bruker advance 400 MHz spectrometer in $CDCl_3$ at room temperature. MALDI-TOF measurements were done on a Voyager-DE PRO from Applied Biosystems using α-cyano-4-hydroxycinnamic acid (CHCA) as the matrix.

RESULTS AND DISCUSSION

The ligand H_2TPPOASH was characterized by UV/vis, ^{1}H NMR, and MS methods. The ^{1}H NMR spectrum is given in the Supporting Information (Figure S1). Au_{22} was characterized by a series of measurements such as UV/vis, steady-state fluorescence, and XPS (36). Figure 1A shows the UV/vis spectra of Au_{25}, Au_{22}, and H_2TPPOASH. Electronic absorption spectra of the quantum clusters show rich features attributed to molecular transitions. The absorption at 672 nm in Au_{25} is due to the intraband transition (HOMO−LUMO) derived from sp orbitals of Au. This position is characteristic of the cluster and occurs in all of the Au_{25} clusters reported so far (36−38, 41−43). In conformity with these reports, various samples reported here show the same features. All of them show the HOMO−LUMO transition at 672 nm.

The formation of porphyrin-anchored Au_{22} was initially characterized by monitoring of the reaction using UV/vis spectroscopy. As time progresses, the so-called intraband transition of Au_{25} diminished in intensity and finally vanished completely. This clearly shows the disappearance of the parent Au_{25}. Simultaneously, we see the emergence of a new peak at 520 nm and a small hump at ~635 nm, which are characteristic of Au_{22} (36). The inset shows the expanded view of the HOMO−LUMO transitions of these two clusters. Surprisingly, the characteristic $\pi-\pi^*$ electronic transitions of the porphyrin moiety were not distinctly observable in Au_{22}, probably because of the merging of the B and Q transitions with the broad absorption features of the cluster (Figure 1A).

Figure 1B shows the PL spectra of $Au_{25}SG_{18}$, Au_{22}, and H_2TPPOASH. Free H_2TPPOASH shows two intense emissions at 650 and 715 nm when excited at 420 nm. The PL spectrum of H_2TPPOASH was taken in toluene, whereas that of the clusters was taken in DI water. The PL studies of Au_{25} were done in great detail and have been reported recently (36−38). Emission of Au_{25} occurs in the range of 600−800 nm with an emission maximum of 700 nm at 535 nm excitation. However, the PL spectrum of porphyrin-anchored Au_{22} shows a broad emission in the 550−850 nm region with 520 nm excitation (Figure 1B). The emission from the cluster shows broad features, and these are masking the features of H_2TPPOAS− because these two occur in the same region. However, the peak at 468 nm in the excitation spectrum of the cluster shows the presence of a porphyrin-anchored (H_2TPPOAS−) moiety on it (see also below). The excitation of H_2TPPOASH at 420 nm is shifted to 468 nm in

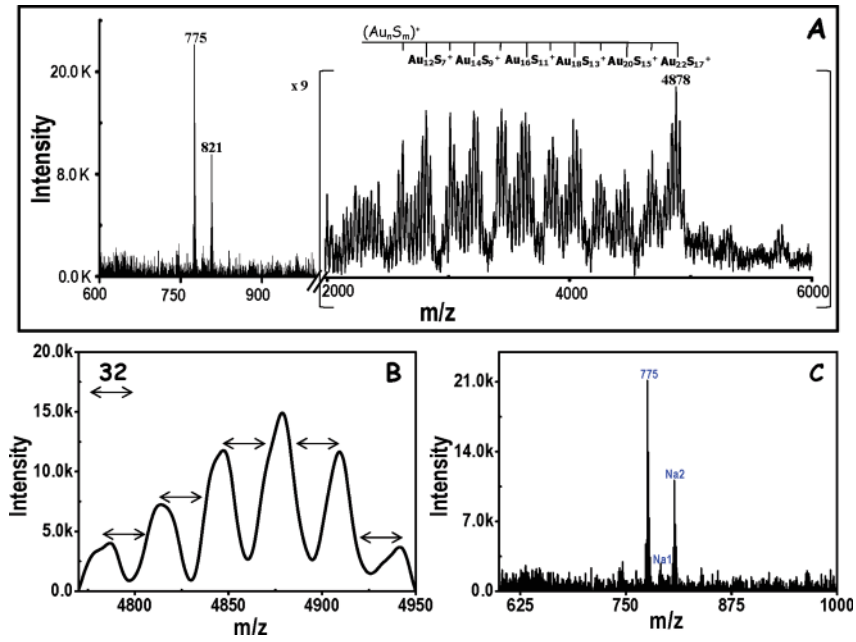

FIGURE 2. (A) MALDI-TOF MS of Au_{22} in the positive mode showing the presence of $Au_{22}S_{17}$. A group of peaks is separated by *m/z* 197, due to gold, between the adjacent major peaks. (B) Expanded view of the last few sets of peaks in part A, showing a separation of *m/z* 32 due to sulfur. (C) Expanded view of the mass spectrum collected in the lower mass region in part A, showing the presence of a H_2TPPOAS− ligand (*m/z* 775) and one and two sodium pickups (marked Na1 and Na2).

the cluster. This could be due to the strong electronic interaction of the porphyrin ligand with the metal core. The peak at 520 nm in the excitation spectrum of Au_{22} is characteristic of the clusters. This excitation shows a blue shift of ~15 nm in comparison to that of Au_{25}. The spectra altogether support the presence of H_2TPPOAS− on the cluster.

The temperature dependence of the solution-state emission from these clusters showed drastic enhancement of fluorescence when the sample is cooled to 5 °C. The emission is also visible by the naked eye under a UV lamp. Figure 1C shows the temperature-dependent emission collected from the sample at room temperature (RT) and at 5 °C. The corresponding photographs of the samples under a UV lamp are also given in Figure 1D. The quantum yield of the cluster is 0.04 at room temperature, using Rhodamine 6G as the reference. This is 20-fold higher than that of parent Au_{25} (quantum yield, 1.9×10^{-3}). This newly developed cluster is highly stable even under daylight. We have irradiated the cluster solution with UV light for a few hours and remeasured the UV/vis and PL. All of the cluster features were still intact.

The role of the concentration and the effect of the alkane chain length of the porphyrinthiol were studied. At a lower concentration of the ligand, we observed parent Au_{25} along with Au_{22}, whereas at higher concentration, we could not see any parent cluster but excess porphyrinthiol could be isolated. This clearly indicates that at a critical concentration all of the parent clusters convert to Au_{22}. We have standardized this concentration and used it for all of our syntheses. The effect of the alkane chain length of the ligand has been studied for two extreme cases. We have tried the cluster synthesis with a phenylporphyrinthiol (−SH is directly attached to the phenyl carbon). Here no reaction was seen. The reaction occurs with the other case tried, namely, that with an alkyl chain with eight carbon atoms (H_2TPPOASH). Thus, we believe that the process will occur only if there are at least a few carbon atoms between the aromatic ring and the −SH group. This situation is similar to self-assembled monolayers of thiols on gold, which need at least two methylene units between −SH and the phenyl ring to form a stable monolayer (60).

To probe the nature of the core and ligands, we measured the MALDI MS data of the cluster using CHCA as the matrix. The laser desorption mass spectrum of clusters such as Au_{25} does not give the integral features of the cluster core along with the ligands (36, 41). However, in favorable cases, the MALDI MS spectra show characteristic features. In the present case, the MALDI MS data show a series of features assignable to $Au_nS_m^+$ with a rapidly disappearing intensity above the Au_{22} peaks. Note that the sample taken for analysis was pure because only one band was seen in PAGE. Thus, the lower mass number features with successive Au losses are attributed to fragmentation and laser-induced dissociation of the clusters. The slight enhancement in the relative intensity of Au_{18} may be attributed to the increased stability of this core in comparison to those of Au_{21}, Au_{20}, and Au_{19}. The MS spectrum shows a peak at *m/z* 4878 (in the higher mass region, the spectrum is multiplied by a factor of 9), assigned to $Au_{22}S_{17}$ (Figure 2A). It is important to note that there is no higher mass number feature of significant intensity above *m/z* 4878. The spectrum is characteristic in the sense that below this peak all of the lower clusters of Au_{21}, Au_{20}, etc., are observed. Laser desorption ionization of gold thiolate clusters and nanoparticles results in C−S bond cleavage (5, 61, 62) and so the peak at *m/z* 4878 can be attributed to $Au_{22}L_{17}$, where L is a thiolate. The peaks around each cluster such as Au_{22}, Au_{21}, etc., are separated

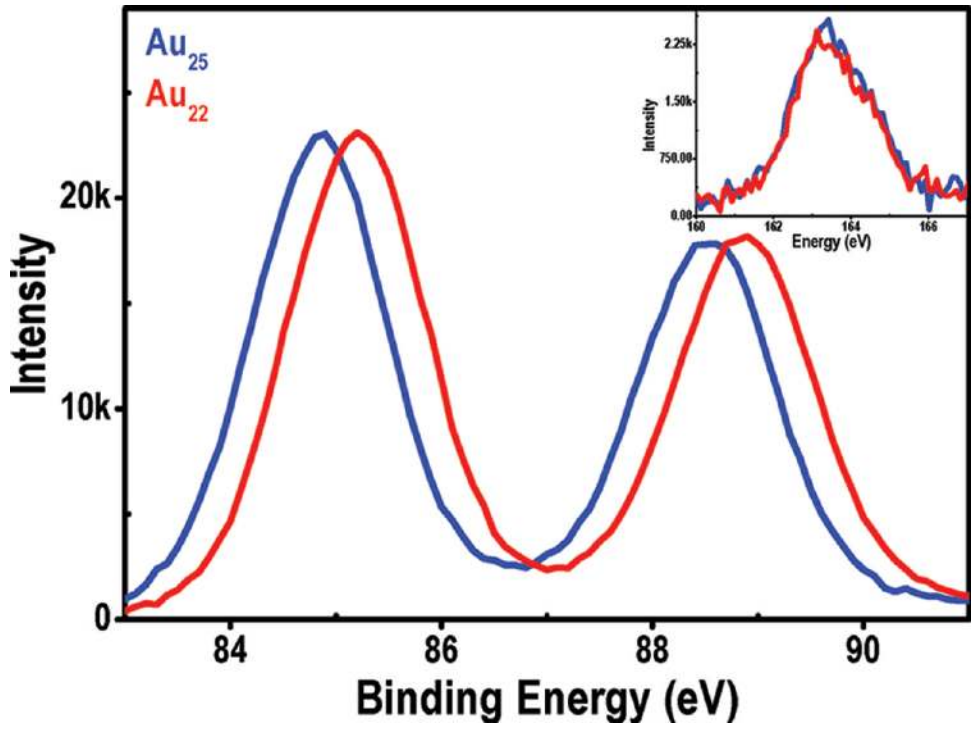

FIGURE 3. Au 4f core level photoemission spectra (normalized) of Au_{25} and Au_{22}. The small shift of BE is attributed to the core reduction. The S 2p (normalized) core levels of these two clusters are given in the inset.

by *m/z* 32 because of sulfur, both above and below the characteristic peak. Desorption-induced clustering and fragmentation are common in laser ionization (61). The *m/z* 32 spacing is a characteristic aspect of every $Au_nS_m^+$ feature observed. An expanded view of this separation is given in Figure 2B. In addition to these clusters, we see a peak at *m/z* 775 in the low mass region due to the H_2TPPOAS− moiety, which picks up two sodium atoms (*m/z* 821, Na2) upon desorption. This region is expanded and given in Figure 2C. The peak due to a single sodium pickup shows only a lower intensity (Na1).

The elemental composition of this cluster was confirmed by CHNS analysis, which supports a molecular composition of $Au_{22}[(SG)_{15}(SAOPPTH_2)_2]$, having two H_2TPPOAS− ligands per cluster (details are in Table 1 in the Supporting Information). We compared the elemental composition of nitrogen in both of the clusters, and it is seen that the percentage of nitrogen in Au_{22} (7.42%) is higher than that in the parent Au_{25} (7.19%) cluster. This clearly shows the presence of porphyrin rings in the compound. EDAX also gives comparable data. The EDAX maps of Au Mα, Au Lα, and S Kα of cluster aggregates are given in the Supporting Information (Figure S2). During the core-etching reaction of Au_{25} clusters with porphyrinthiol, we selectively harvested Au_{22} clusters. The exact reason for the formation of Au_{22} is not known, but one of the possible reasons could be its stability. Tsukuda et al. synthesized a series of GSH-protected clusters and determined their chemical composition by ESI-MS (36). These clusters are $Au_{10}(SG)_{10}$, $Au_{15}(SG)_{13}$, $Au_{18}(SG)_{14}$, $Au_{22}(SG)_{16}$, $Au_{22}(SG)_{17}$, $Au_{25}(SG)_{18}$, $Au_{29}(SG)_{20}$, $Au_{33}(SG)_{22}$, and $Au_{39}(SG)_{24}$. All of these nine clusters have good stability. Here Au_{22} is the cluster preceding Au_{25}. Hence, during the etching reaction of Au_{25} with thiol, it is likely that the next stable lower size is formed.

The core reduction was proven by a comparison of the XPS data of Au_{25} and Au_{22}. Figure 3 shows the photoelectron spectra of the samples in the 4f region. The $4f_{7/2}$ and $4f_{5/2}$ BEs of gold in Au_{25} are 84.8 and 88.5 eV, respectively. However, in the case of Au_{22}, these peaks were shifted to 85.2 and 88.9 eV. A positive shift of 0.4 eV could be attributed to the core reduction, which matches with the data reported for Au_{22} (37). The S 2p of these two clusters were also measured, and the data are given in the inset of Figure 3. From the XPS data, we find the Au/S atomic ratio to be 1.32, which is in agreement with a composition of $Au_{22}S_{17}$ (the expected value is 1.30). The S 2p occurs at a slightly higher BE (163.2 eV) than typical thiolates (∼162.0 eV). The O 1s and N 1s regions were also examined, and these are given in the Supporting Information (Figure S3). The O 1s of Au_{22} shows a shift to higher BE compared to that of Au_{25}, possibly because of the presence of oxygen bridging the macrocyclic porphyrin ring and the long-chain alkyl chain.

The presence of porphyrin (H_2TPPOAS−) on the cluster core is confirmed by a simple fluorimetric titration. We started the PL studies with the cluster solution alone. Immediately after the first set of measurements, 20 μL of 10^{-6} M Zn^{2+} ions was added. The solution was sonicated for 1 min at room temperature. The PL of these mixtures shows a decrease in fluorescence at 670 nm. In addition to this, a new peak at ∼550 nm and a broad emission extending until 800 nm were observed, and these are perhaps due the emission from the ZnTPPOAS complex (63). The PL spectra were collected by adding 150 and 300 μL of the same solution. Finally, all of the fluorescence from the cluster was

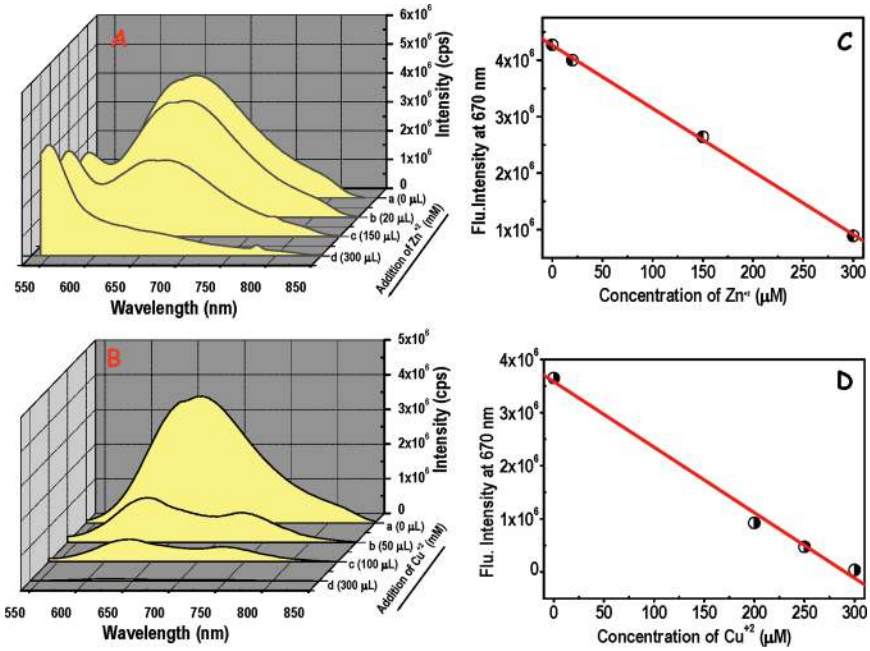

FIGURE 4. (A and B) PL spectra of the red cluster during fluorimetric titration with Zn^{2+} and Cu^{2+}, respectively. (C and D) Plot of the fluorescent intensity of the cluster at 670 nm with the concentration of Zn^{2+} and Cu^{2+}, respectively.

quenched, and only these new emissions were left (Figure 4A). The same set of fluorimetric titrations were done using Cu^{2+} ions also. However, in this case, upon the first addition of Cu^{2+} ions (~50 μL of 10^{-6} M), the fluorescence from the cluster was quenched and the broad band was resolved into two separate emissions at 650 and 715 nm; these positions are similar to those of the parent H_2TPPOASH at 420 nm excitation (see Figure 1B). No new peaks were observed. The experiment was continued with 200 and 300 μL of the same solution. Finally, all of the emission got quenched completely (Figure 4B). It is known that the ZnTPP complex exhibits emission maxima at 600 and 656 nm, depending on the substitution, whereas the CuTPP complex has no such effect on the emission maximum, but it will quench the TPP fluorescence gradually (63). Altogether the data clearly establish the presence of H_2TPPOAS− on the gold core. In both of these cases, we plotted the fluorescence intensity versus the concentration of ions (Figure 4C,D). Data are in good agreement with the first-order kinetics. The kind of interaction of these two metal ions with a porphyrin-functionalized cluster is entirely different. The addition of Cu^{2+} leads to the direct quenching of the cluster PL because there is no possible emission from the CuTPP complex, whereas in the case of Zn^{2+}, we could see quenching of the cluster PL and the appearance of a new emission at ~550 nm due to the formation of the fluorescent ZnTPP complex. The CuTPP complex is paramagnetic and nonfluorescent (phosphorescent), whereas the ZnTPP complex is diamagnetic and fluorescent. This fluorimetric titration helps to understand the nature of the metal ions, namely, whether it is paramagnetic or diamagnetic.

The fluorescence decays of Au_{22} (in water) and H_2TPPOASH (in toluene) were measured using a picosecond-resolved, time-correlated, single-photon-counting (TCSPC) technique. The decay profile of Au_{22} (at 409 nm excitation) is given in Figure 5. The inset of the figure shows the decay profile of H_2TPPOASH. Lifetime values of the clusters were obtained by numerical fitting of the fluorescence at 630 nm. Lifetimes of Au_{22} are 0.05 ns (86.50%), 1.16 ns (6.60%), 9.59 ns (3.50%), and 141.80 ns (3.40%). The lifetime values of H_2TPPOASH are 9.15 (70%) and 1.24 (30%), respectively (table, given in the inset). To deconvoluate the contribution of the porphyrin moiety anchored to the Au_{22} cluster, we have measured the fluorescence decay of the Au_{22} cluster at 600 nm, where the contribution of the porphyrin emission is negligibly small (Figure 1B), and also at 650 nm, where the porphyrin emission is prominent (Figure 1B). However, the similarity of the lifetime components (Table 2 and Figure S5 in the Supporting Information) in the two detected wavelengths (600 and 650 nm) reveals that emission of the cluster is coming predominantly from the Au_{22} itself. We have also excited the cluster by 445 nm wavelength, which is close to the 468 nm absorption [note that the absorption band (Figure 1B) of H_2TPPOASH at 420 nm is shifted to 468 nm in the cluster]. Here also we detected fluorescence at 600 and 650 nm (Figure S5 in the Supporting Information and Table 2), and the time constants are found to be similar to that of 409 nm excitation. The lifetime component from the ligand present in the cluster is almost absent even though there are two porphyrin moieties per cluster (the presence of the ligand is proven by quenching studies and elemental analysis). It is already known that the binding of thiolated fluorophores on gold nanoparticles produces strong, structure-dependent static quenching of the fluorescence intensity (64, 65). In this present system also, we could see a drastic decrease of the 468 nm peak intensity (ligand absorption) in the excitation spectrum of the cluster (Figure 1B). This altogether indicates the presence of a strong electronic interaction between the ligand and the metal core. Moreover, the lifetime measurements were done in high concen-

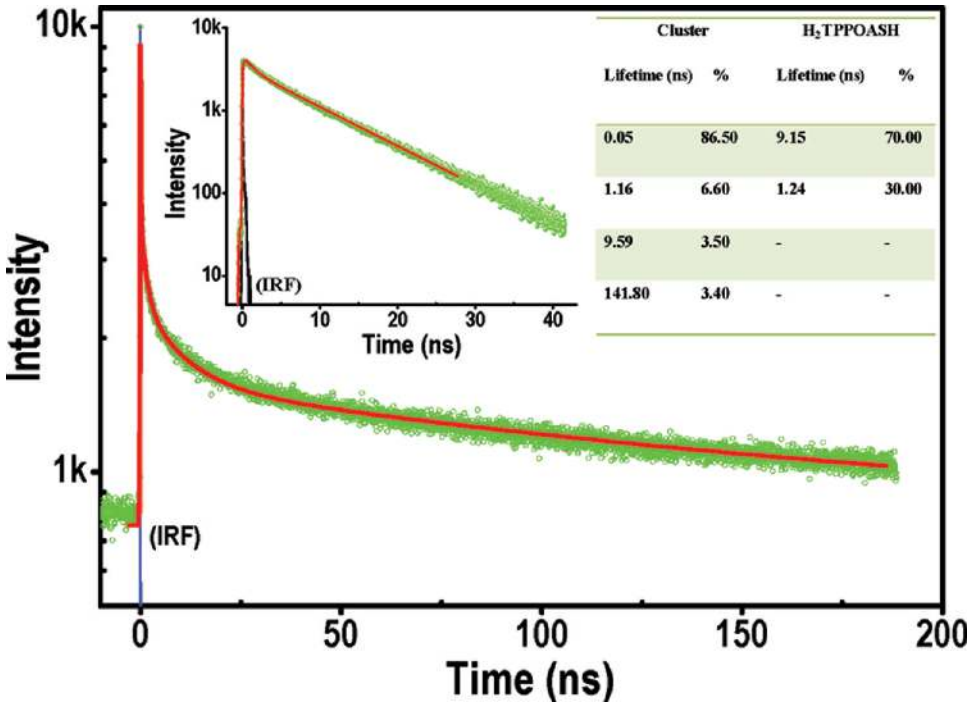

Cluster		H_2TPPOASH	
Lifetime (ns)	%	Lifetime (ns)	%
0.05	86.50	9.15	70.00
1.16	6.60	1.24	30.00
9.59	3.50	-	-
141.80	3.40	-	-

FIGURE 5. Fluorescence decay of Au_{22} in water. The inset shows the decay profile of H_2TPPOASH in toluene. The lifetime values of porphyrin-anchored Au_{22} and H_2TPPOASH are given in the table. The IRF shows a resolution of 80 ps.

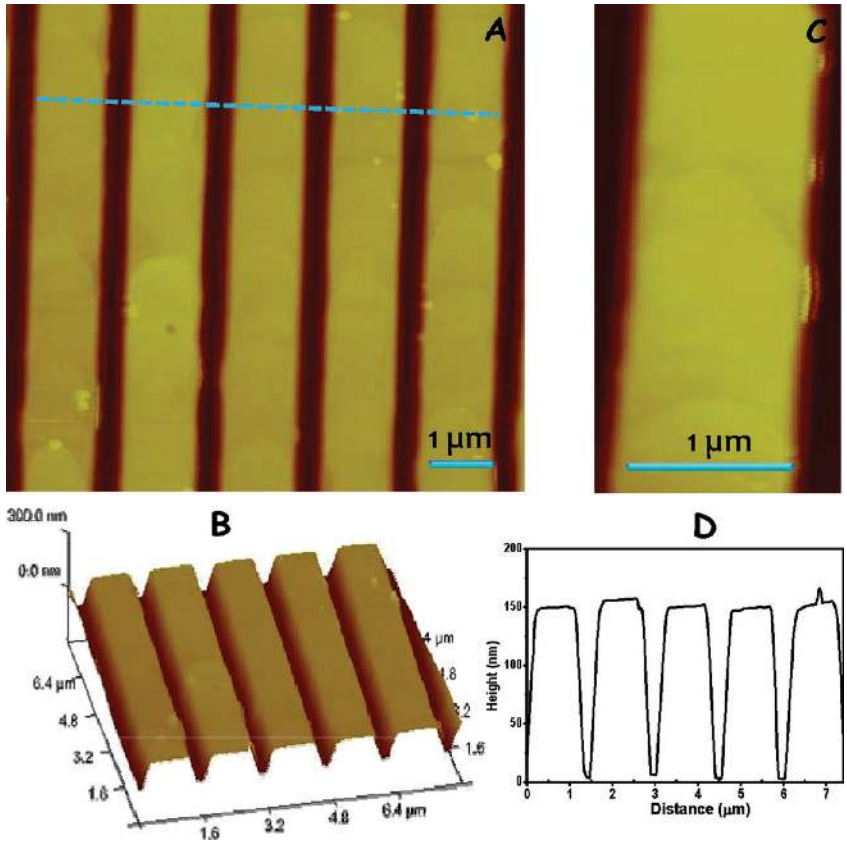

FIGURE 6. (A) Tapping-mode AFM image of a large area pattern of Au_{22} created by the PDMS stamp method. (B) Corresponding 3D image showing the spacing more clearly. (C) AFM image of a single line. (D) Corresponding height profile from the region shown in the AFM image in part A. The height and width of the patterned lines are around 140 nm and 1.2 μm, respectively.

tration, which will also facilitate the self-quenching of fluorophores.

We also studied the solid-state emission from these clusters using a Raman spectrometer with 532 nm excitation. The solid-state emission of the cluster exactly matches the solution-state emission. However, there is a small red shift of the emission maximum that could be attributed to the solid-state effects. An interesting nature of these types

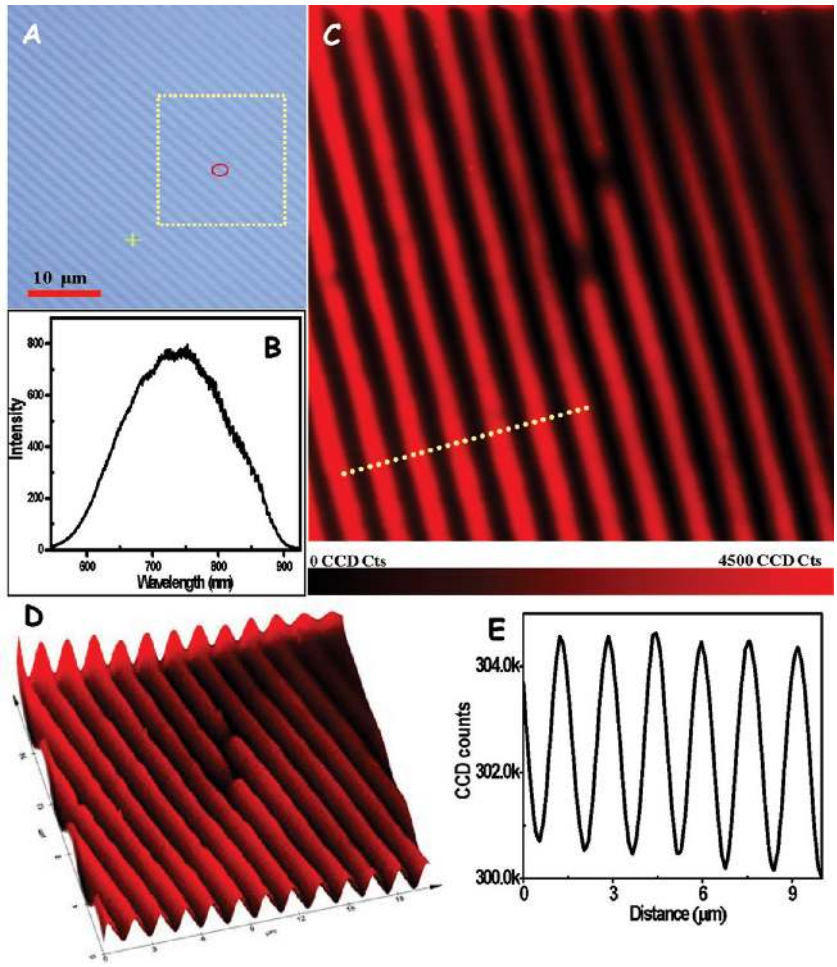

FIGURE 7. (A) Optical image (under white-light illumination) of the Au_{22} patterns. (B) Fluorescence spectrum collected using a 532 nm laser showing an emission maximum of 700 nm. (C) Fluorescence image of the regular and periodic patterns collected from the area selected by a rectangular box in part A (20 μm × 18 μm). (D) Corresponding 3D image. (E) Fluorescence intensity profile (CCD counts vs distance in micrometers) collected from the regions marked by a dashed line in part C.

of clusters is their intense emission even in the solid state. The fluorescence from these clusters was mapped using the emission peak at 700 nm. The solid-state fluorescence images and the corresponding 3D images are given in Supporting Information (Figure S4). In this image, the regions in red and black have maximum and minimum fluorescence intensities, respectively.

We utilized the solid-state emission from the clusters to produce fluorescent patterns by soft lithography. Details of the pattern development are given in the Experimental Section. We measured AFM images of these patterns in the tapping mode, which shows the presence of the clusters. The spacing between the channels is around 1 μm, which is in accordance with AFM images of the stamp (see Scheme 3). Figure 6A shows a tapping-mode AFM image of the patterns made with the clusters. These features show a regular pattern over a wide area. The corresponding 3D image is given in Figure 6B. The height profile (Figure 6D) was collected along the line drawn across the patterns, shown in Figure 6A. The spacing between the cluster patterns is better visible in 3D images. The height of each line is ~140 nm. We also imaged AFM of a single line, given in Figure 6C. Here we can clearly see patterning in the micrometer regime, with nanometer resolution with respect to its edges.

The Fluorescence image and corresponding spectrum of Au_{22} patterns were collected using confocal Raman spectroscopy. The patterns were developed over a thin glass plate and mounted on a piezo-equipped scan stage to enable spectral imaging. For fluorescence imaging, we selected an area and focused the laser beam on the surface of the pattern. A white-light image of the Au_{22} pattern, selected for fluorescence imaging, was collected (Figure 7A; the area in the rectangular box was used for imaging). The fluorescence collected using a 532 nm laser showed an emission maximum of 700 nm (Figure 7B). The fluorescence image of the patterns was collected using the same excitation laser. The integration time used for imaging was 0.05 s for a scan width of 20 μm × 18 μm. Figure 7C shows the fluorescence image of the Au_{22} pattern. Here the regions in red indicate the presence of the cluster, and those in black indicate the blank region (initially occupied by the PDMS stamp; see Figure S6 in the Supporting Information). The corresponding 3D image is given in Figure 7D. The intensity profile collected from the regions marked by a dashed line drawn in the corresponding fluorescence image is given in Figure 7E. In comparison with the AFM image, the fluorescent patterns appear rounded because of the diffraction limit of optical imaging.

Various studies presented here suggest that a new class of fluorescent molecular clusters of gold can be made with diverse chemical functionalities in a single step using well-characterized Au_{25} as a precursor. The present study, in conjunction with the previous reports from our group on functionalized Au_{25}, suggests that the electronic structure of the metal core in such clusters is unaltered during covalent functionalization. In the case of Au_{25}, we had shown that various ligands do not alter the optical absorption and fluorescence spectra significantly (41). It is important to note that, even with the functionalization using an electron-rich porphyrinthiol, the optical absorption and emission features of Au_{22} are not affected significantly. Thus, the thiolated core behaves like an isolated entity in its electronic features. This inference is important in the application of such materials. The chemistry and material science of such clusters are unlikely to be influenced by the ligand shell, although it allows chemical diversity. The prepared clusters are patternable with high resolution. This aspect is particularly important when they are used for an optical diffraction-based diagnosis (66).

CONCLUSIONS

We synthesized NIR-emitting gold clusters, with a high quantum yield, from a well-characterized subnanocluster ($Au_{25}SG_{18}$) by a combined core reduction/ligand-exchange protocol at a liquid−liquid interface. The prepared cluster was characterized by UV/vis, steady-state fluorescence, MALDI-TOF MS, SEM, elemental analysis, and XPS. The presence of a TPPOAS− moiety on the cluster surface was confirmed by a simple fluorimetric titration using Zn^{2+} and Cu^{2+} ions. The quenching of fluorescence with Zn^{2+} and Cu^{2+} shows the possible application of these materials for the selective detection of metal ions. The number of H_2TPPOAS− moieties per cluster was calculated to be around two. Intense fluorescence from these clusters was employed to produce fluorescing patterns using soft lithography over a micrometer regime with nanometric sharpness, of importance in optical devices. The patterns were mapped using tapping-mode AFM. The line width is found to be around 1.2 μm, in accordance with the spacing in the PDMS stamp developed from the master. The fluorescence of these patterns was mapped over a large area using a Raman microscope at 532 nm excitation. Such patterns demonstrate possible applications in the selective detection of bio molecules, cells, etc., following an appropriate functionalization of the cluster.

Acknowledgment. We thank the Nanoscience and Nano Mission of Department of Science and Technology (DST), Government of India, for constantly supporting our research program. E.S.S. thanks the University Grants Commission, and B.R. thanks CSIR for research fellowships.

Supporting Information Available: (1) Details of PDMS stamp preparation, (2) ^{1}H NMR spectrum of H_2TPPOASH, (3) elemental analysis data of $Au_{22}[(SG)_{15}(H_2TPPOAS)_2]$, (4) an EDAX spectrum and elemental mapping of Au_{22}, (5) O 1s and N 1s of Au_{22} and Au_{25}, (6) an inherent solid-state fluorescence image of an Au_{22} aggregate, (7) fluorescence transients of porphyrin-anchored Au_{22} at 600 and 650 nm (λ_{ex} = 409 nm) and 600 and 650 nm (λ_{ex} = 445 nm), (8) a table containing the lifetime components of clusters in different excitation and emission wavelengths, and (9) a FESEM image of a PDMS stamp. This material is available free of charge via the Internet at http://pubs.acs.org.

REFERENCES AND NOTES

(1) Bigioni, T. P.; Whetten, R. L.; Dag, Ö. *J. Phys. Chem. B* **2000**, *104*, 6983–6986.
(2) Huang, T.; Murray, R. W. *J. Phys. Chem. B* **2001**, *105*, 12498–12502.
(3) Peyser, L. A.; Vinson, A. E.; Bartko, A. P.; Dickson, R. M. *Science* **2001**, *291*, 103–106.
(4) Crespo, P.; Litran, R.; Rojas, T. C.; Multigner, M.; de la Fuente, J. M.; Sanchez-Lopez, J. C.; Garcia, M. A.; Hernando, A.; Penades, S.; Fernandez, A. *Phys. Rev. Lett.* **2004**, *93*, 087204.
(5) Schaaff, T. G.; Whetten, R. L. *J. Phys. Chem. B* **2000**, *104*, 2630–2641.
(6) Tsunoyama, H.; Sakurai, H.; Ichikuni, N.; Negishi, Y.; Tsukuda, T. *Langmuir* **2004**, *20*, 11293–11296.
(7) Tsunoyama, H.; Sakurai, H.; Negishi, Y.; Tsukuda, T. *J. Am. Chem. Soc.* **2005**, *127*, 9374–9375.
(8) Chen, S.; Ingram, R. S.; Hostetler, M. J.; Pietron, J. J.; Murray, R. W.; Schaaff, T. G.; Khoury, J. T.; Alvarez, M. M.; Whetten, R. L. *Science* **1998**, *280*, 2098–2101.
(9) Whetten, R. L.; Shaligullin, M. N.; Khouury, J. T.; Schaaff, T. G.; Vermar, I.; Alvarez, M. M.; Willkinson, A. *Acc. Chem. Res.* **1999**, *32*, 397–406.
(10) Huang, T.; Murray, R. W. *J. Phys. Chem. B* **2001**, *105*, 12498–12502.
(11) Schwerdtfeger, P. *Angew. Chem., Int. Ed.* **2003**, *42*, 1892–1895.
(12) Cui, Y.; Ren, B.; Jao, J. L.; Gu, R. A.; Tian, Z. Q. *J. Phys. Chem. B* **2006**, *110*, 4002–4006.
(13) Bruchez, M., Jr.; Moronne, M.; Gin, P.; Weiss, S.; Alivisatos, A. P. *Science* **1998**, *281*, 2013–2016.
(14) Prasad, P. N. *Nanophotonics*; Wiley: Hoboken, NJ, 2004.
(15) Arya, H.; Kaul, Z.; Wadhwa, R.; Taira, K.; Hirano, T.; Kaul, S. C. *Biochem. Biophys. Res. Commun.* **2005**, *329*, 1173–1177.
(16) Liu, W.; Choi, H. S.; Zimmer, J. P.; Tanaka, E.; Frangioni, J. V.; Bawendi, M. *J. Am. Chem. Soc.* **2007**, *129*, 14530–14531.
(17) Liu, W.; Howarth, M.; Greytak, A. B.; Zheng, Y.; Nocera, D. G.; Ting, A. Y.; Bawendi, M. G. *J. Am. Chem. Soc.* **2008**, *130*, 1274–1284.
(18) Derfus, A. M.; Chan, W. C. W.; Bhatia, S. N. *Nano Lett.* **2004**, *4*, 11–18.
(19) Medintz, I. L.; Clapp, A. R.; Mattoussi, H.; Goldman, E. R.; Fisher, B.; Mauro, J. M. *Nat. Mater.* **2003**, *2*, 630–638.
(20) Lin, C.-A. J.; Yang, T.-Y.; Lee, C.-H.; Huang, S. H.; Sperling, R. A.; Zanella, M.; Li, J. K.; Shen, J.-L.; Wang, H.-H.; Yeh, H.-I.; Parak, W. J.; Chang, W. H. *ACS Nano* **2009**, *3*, 395–401.
(21) Sperling, R. A.; Gil, P. R.; Zhang, F.; Zanella, M.; Parak, W. *Chem. Soc. Rev.* **2008**, *37*, 1896–1908.
(22) Pumera, M.; Castaneda, M. T.; Pividori, M. L.; Eritja, R.; Merkoci, A.; Alegret, S. *Langmuir* **2005**, *21*, 9625–9629.
(23) Zheng, J.; Nicovich, P. R.; Dickson, R. M. *Annu. Rev. Phys. Chem.* **2007**, *58*, 409–431.
(24) Zheng, J.; Petty, J. T.; Dickson, R. M. *J. Am. Chem. Soc.* **2003**, *125*, 7780–7781.
(25) Zheng, J.; Zhang, C. W.; Dickson, R. M. *Phys. Rev. Lett.* **2004**, *93*, 077402.
(26) Duan, H.; Nie, S. *J. Am. Chem. Soc.* **2007**, *129*, 2412–2413.
(27) Bartlett, P. A.; Bauer, B.; Singer, S. *J. Am. Chem. Soc.* **1978**, *100*, 5085–5089.
(28) Menard, L. D.; Gao, S.-P.; Xu, H.; Twesten, R. D.; Harper, A. S.; Song, Y.; Wang, G.; Douglas, A. D.; Yang, J. C.; Frenkel, A. I.; et al. *J. Phys. Chem. B* **2006**, *110*, 12874–12883.
(29) Schmis, G.; Boese, R.; Pfeil, B.; Andermann, F.; Meyer, S.; Calis, G. H. M.; Van der Velden, J. W. A. *Chem. Ber.* **1981**, *114*, 3634–3642.
(30) Peyser, L. A.; Vinson, A. E.; Bartko, A. P.; Dickson, R. M. *Science* **2001**, *291*, 103–106.

(31) (a) Petty, J. T.; Zheng, J.; Hud, N. V.; Dickson, R. M. *J. Am. Chem. Soc.* **2004**, *126*, 5207–5212. (b) Patel, S. A.; Richards, C. I.; Hsiang, J.; Dickson, R. M. *J. Am. Chem. Soc.* **2008**, *130*, 11602–11603. (c) Ritchie, C. M.; Johnsen, K. R.; Kiser, J. R.; Antoku, Y.; Dickson, R. M.; Jetty, P. J. T. *J. Phys. Chem. C* **2007**, *111*, 175–181. (d) Richards, C. I.; Choi, S.; Hsiang, J. C.; Antoku, Y.; Vosch, T.; Bongiorno, A.; Tzeng, Y. L.; Dickson, R. M. *J. Am. Chem. Soc.* **2008**, *130*, 5038–5039.
(32) (a) Zheng, J.; Dickson, R. M. *J. Am. Chem. Soc.* **2002**, *124*, 13982–13983. (b) Sun, X.; Dong, S.; Wang, E. *Macromolecules* **2004**, *37*, 7105–7108.
(33) Zhang, J. G.; Xu, S. Q.; Kumacheva, E. *Adv. Mater.* **2005**, *17*, 2336–2340.
(34) Ledo-Surez, A.; Rivas, J.; Rodrguez-Abreu, C. F.; Rodrguez, M. J.; Pastor, E.; Hernndez-Creus, A.; Oseroff, S. B.; Lopez-Quintela, M. A. *Angew. Chem., Int. Ed.* **2007**, *46*, 8823–8827.
(35) Schaaff, T. G.; Knight, G.; Shafigullin, M. N.; Borkman, R. F.; Whetten, R. L. *J. Phys. Chem. B* **1998**, *102*, 10643–10646.
(36) Negishi, Y.; Nobusada, K.; Tsukuda, T. *J. Am. Chem. Soc.* **2005**, *127*, 5261–5270.
(37) Shichibu, Y.; Negishi, Y.; Tsukuda, T.; Teranishi, T. *J. Am. Chem. Soc.* **2005**, *127*, 13464–12465.
(38) Shichibu, Y.; Negishi, Y.; Tsunoyama, H.; Kanehara, M.; Teranishi, T.; Tsukuda, T. *Small* **2007**, *3*, 835–839.
(39) Muhammed, M. A. H.; Pradeep, T. *Chem. Phys. Lett.* **2007**, *449*, 186–190.
(40) Zhu, M.; Aikens, C. M.; Hollander, F. J.; Schatz, G. C.; Jin, R. *J. Am. Chem. Soc.* **2008**, *130*, 5883–5885.
(41) Shibu, E. S.; Muhammed, M, A, H.; Tsukuda, T.; Pradeep, T. *J. Phys. Chem. C* **2008**, *112*, 12168–12176.
(42) Shibu, E. S.; Pradeep, T. *Int. J. Nanosci.* **2009**, *2*, 223–226.
(43) Muhammed, M. A. H.; Shaw, A. K.; Pal, S. K.; Pradeep, T. *J. Phys. Chem C* **2008**, *112*, 14324–14330.
(44) Muhammed, M. A. H.; Ramesh, S.; Sinha, S. S.; Pal, S. K.; Pradeep, T. *Nano Res.* **2008**, *1*, 333–340.
(45) Zhu, M.; Qian, H.; Jin, R. *J. Am. Chem. Soc.* **2009**, *131*, 7220–7221.
(46) Mrudula, K. V.; Udaya Bhaskara Rao, T.; Pradeep, T. *J. Mater. Chem.* **2009**, *19*, 4335—4342.
(47) Xie, J.; Zheng, Y.; Ying, J. Y. *J. Am. Chem. Soc.* **2009**, *131*, 888–889.
(48) Chirico, G.; Cannone, F.; Diaspro, A.; Bologna, S.; Pellegrini, V.; Nifosi, R.; Beltram, F. *Phys. Rev. E* **2004**, *70*, 030901.
(49) Cinelli, R. A. G.; Pellegrini, V.; Ferrari, A.; Faraci, P.; Nifosi, R.; Tyagi, M.; Giacca, M.; Beltram, F. *Appl. Phys. Lett.* **2001**, *79*, 3353–3355.
(50) de la Fuente, J. M.; Andar, A.; Gadegaard, N.; Berry, C. C.; Kingshott, P.; Riehle, M. O. *Langmuir* **2006**, *22*, 5528–5532.
(51) Xia, Y. N.; Rogers, J. A.; Paul, K. E.; Whitesides, G. M. *Chem. Rev.* **1999**, *99*, 1823–1848.
(52) Nakano, T.; Hsu, Y. H.; Tang, W. C.; Suda, T.; Lin, D.; Koujin, T.; Haraguchi, T.; Hiraoka, Y. *3rd IEEE Int. Conf. Nano/Micro Engineered Mol. Syst., NEMS* **2008**, 476–479.
(53) Bossinger, O.; Schierenberg, E. *Int. J. Dev. Biol.* **1996**, *40*, 431–439.
(54) Xia, Y.; Whitesides, G. M. *Angew. Chem., Int. Ed.* **1998**, *37*, 550–575.
(55) Radha, B.; Kulkarni, G. U. *ACS Appl. Mater. Interfaces* **2009**, *1*, 257–260.
(56) Gates, B. D.; Xu, Q.; Love, J. C.; Wolfe, D. B.; Whitesides, G. M. *Annu. Rev. Mater. Res.* **2004**, *34*, 339–372.
(57) Rao, P. D.; Dhanalekshmi, S.; Littler, B. J.; Lindsey, J. S. *J. Org. Chem.* **2000**, *65*, 7323–7344.
(58) Bhyrappa, P.; Krishnan, V. *J. Chem. Sci.* **2004**, *116*, 71–78.
(59) Hu, J.; Fox, M. A. *J. Org. Chem.* **1999**, *64*, 4959–4961.
(60) Sandhyarani, N.; Pradeep, T. *Int. Rev. Phys. Chem.* **2003**, *22*, 221–262.
(61) Cyriac, J.; Rajeevkumar, V. R.; Pradeep, T. *Chem. Phys. Lett.* **2004**, *390*, 181–185.
(62) Schaaff, T. G. *Anal. Chem.* **2004**, *76*, 6187–6196.
(63) Spellane, P. J.; Gouterman, M.; Antipas, A.; Kim, S.; Liu, Y. C. *Inorg. Chem.* **1980**, *19*, 386–391.
(64) Dulkeith, E.; Morteani, A. C.; Niedereichholz, T.; Klar, T. A.; Feldmann, J.; Levi, S. A.; Van Veggel, F. C. J. M.; Reinhoudt, D. N.; Motter, M.; Gittens, D. I. *Phys. Rev. Lett.* **2002**, *89*, 203002.
(65) Nishida, N.; Shibu, E. S.; Yao, H.; Oonishi, T.; Kimura, K.; Pradeep, T. *Adv. Mater.* **2008**, *20*, 4719–4723.
(66) Acharya, G.; Chang, C.-L.; Holland, D. H.; Thompson, D. H.; Savran, C. A. *Angew. Chem., Int. Ed.* **2008**, *47*, 1051–1053.

AM900350R